ENGINEERING Information Technology & Electronic Engineering
https://www.academax.com/EITEE; https://www.engineering.org.cn
https://ieeexplore.ieee.org/xpl/RecentIssue.jsp?punumber=11344065
E-mail: eng.itee@zju.edu.cn

Available on IEEE Xplore

Research Article
https://doi.org/10.1631/ENG.ITEE.2026.0058

Power amplifier linearization architecture with complementary filtering for broadband signal transmission

Huihui FEI[1], Yucheng YU[2], Peng CHEN[1], Chao YU[1,3]✉

[1] *State Key Laboratory of Millimeter Waves, Southeast University, Nanjing 210096, China*
[2] *Department of Electrical and Electronic Engineering, The Hong Kong Polytechnic University, Hong Kong 999077, China*
[3] *Purple Mountain Laboratories, Nanjing 211111, China*

Abstract: This paper proposes a power amplifier (PA) linearization architecture with complementary filtering to realize high-linearity broadband signal transmission. The architecture fully leverages the advantages of analog and digital filtering techniques, ensuring high harmonic suppression within a compact size and reducing the demand for digital resources. A miniaturized triple-mode bandpass filter (BPF) with a wide stopband is integrated, which effectively suppresses the harmonic components of the PA output. Meanwhile, digital filtering is employed to mitigate intermodulation distortion (IMD) that cannot be effectively suppressed by the integrated analog filter, thus forming a complementary filtering digital predistortion (CF-DPD). As the CF-DPD herein focuses only on addressing the residual distortion left by analog filtering, it naturally reduces the system's sampling rate requirements. Experimental results demonstrate that the proposed filtering power amplifier with integrated feedback port (FPA-FB) delivers 38.7–40.5 dBm output power, 8.4–11.9 dB gain, and a peak power-added efficiency (PAE) of 42.6%–52.1%. The prototype occupies an overall size of 67 mm×32 mm, corresponding to $1.1\lambda_g \times 0.5\lambda_g$, indicating a compact implementation. Moreover, when transmitting a 400-MHz 5G new radio (NR) signal, the system achieves a normalized mean square error (NMSE) of −32.2 dB and an adjacent channel leakage ratio (ACLR) of −45.1/−47.2 dBc at a reduced sampling rate of 850 mega samples per second (MSPS).

Key words: Broadband linearization; Digital predistortion; Multimode filter; Power amplifier (PA)

1 Introduction

With the rapid advancement of wireless communication technologies, signal transmission rates and bandwidths have significantly increased in recent years. For instance, 5G new radio (NR) enables the support of channel bandwidths ranging from 100 MHz to 400 MHz by leveraging advanced carrier aggregation techniques (3GPP, 2024a, 2024b). This increase in broadband transmission demands, driven by higher data rates and the need for more efficient spectrum utilization, has introduced significant challenges in maintaining the linearity of power amplifiers (PAs) within communication systems (Chen SZ and Kang, 2018). The transmission of broadband signals, which contain multiple frequency components, inevitably leads to the generation of intermodulation distortion (IMD). These intermodulation products cause spectral spreading, which results in a degradation of crucial performance metrics such as the adjacent channel leakage ratio (ACLR) and the error vector magnitude (EVM), both of which are essential for evaluating the quality of the transmitted signal. Furthermore, PAs typically operate at high output power levels to sustain efficiency, which intensifies nonlinearities and results in more severe harmonic distortion.

Therefore, the nonlinearity of PA is categorized into two main types here: IMD occurring near the transmission passband and harmonic distortion appearing away from the passband (Fig. 1). To address PA distortion, both analog methods (e.g., filters or feedback circuits) and digital methods (e.g., digital predistortion) are commonly employed. However, neither approach alone is sufficient for comprehensive correction. For both narrowband and broadband PAs, it is necessary to cascade a bandpass or lowpass filter after the PA to suppress

✉ Chao YU, chao.yu@seu.edu.cn
Huihui FEI, https://orcid.org/0009-0008-3395-4712
Yucheng YU, https://orcid.org/0000-0003-4314-8024
Peng CHEN, https://orcid.org/0000-0002-2757-2549
Chao YU, https://orcid.org/0000-0002-3710-460X
CLC number: TN722.75

Received: Mar. 3, 2026; Revision accepted: June 2, 2026;
Crosschecked: June 10, 2026

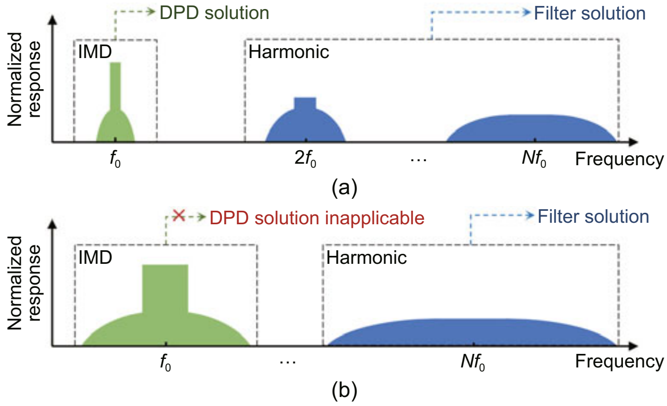

Fig. 1 Distortion mitigation solutions for narrowband (a) and broadband (b) power amplifiers. IMD: intermodulation distortion; DPD: digital predistortion

harmonic distortion. However, as the signal bandwidth increases, the digital predistortion (DPD) solution for suppressing IMD becomes increasingly impractical due to the continuously growing demands on the sampling rate and computational resources. Therefore, for broadband signal transmission scenarios, it is essential to better leverage digital and analog filtering techniques and propose a more effective architecture.

As a representative analog technique, filters are commonly used to suppress unwanted frequency components and improve signal purity. Filters come in a wide variety of types, each with distinct spectral characteristics. For example, widestopband filters can attenuate harmonic components, while narrowband bandpass filters (BPFs), such as film bulk acoustic resonator (FBAR) filters (Menendez et al., 2006; Zhu XE et al., 2009; Nam et al., 2021; Liang et al., 2025), surface acoustic wave (SAW) filters (Ruppel et al., 2002; Ruppel, 2017), and evanescent-mode filters (Joshi et al., 2007; Park et al., 2009), can be used to address IMD. However, analog filters often face challenges in achieving precise frequency control. Specifically, attaining sharp roll-off characteristics typically requires high Q-factors (quality factors) or higher-order filter designs. High Q-factors usually lead to increased insertion loss, which can significantly reduce PA efficiency, and higher-order filters often involve multiple resonators, making filters too bulky for effective integration into compact communication systems.

As a representative digital technique for addressing nonlinearity, DPD has been widely adopted due to its precise control and effective mitigation of distortion (Zhu AD, 2015; Katz et al., 2016; Wood, 2017; Liu et al., 2020; Othmani et al., 2023). On one hand, DPD provides an effective method for correcting PA nonlinearity without compromising system efficiency. On the other hand, DPD can mitigate IMD within the main channel, a task that analog filters are incapable of performing. Despite its advantages, DPD becomes increasingly demanding in terms of the sampling rate as the signal bandwidth expands. To overcome this limitation, band-limited DPD (BL-DPD) was proposed by Yu et al. (2012), which alleviates the high sampling rate requirements while maintaining the accuracy of nonlinear distortion correction. This suggests a direction for high-linearity broadband signal transmission but remains a preliminary solution because it is based on a symmetrical filtering function, while filters in practical applications may not exhibit symmetrical frequency distributions, as demonstrated in Yu et al. (2012).

In this paper, we propose a PA linearization architecture with complementary filtering that achieves full-band distortion suppression by efficiently allocating analog and digital resources. This architecture first uses the analog filtering technique to suppress distortion to the greatest extent possible. Then, it employs a digital filtering technique to suppress frequency bands outside the stopband of the analog filters, effectively eliminating any residual distortion. To demonstrate this concept, this paper integrates analog filtering resources into PA design, thus forming a filtering PA. Compared with conventional architectures using separate PA, filter, and feedback coupler blocks, this implementation reduces the number of discrete radio frequency (RF) components and lowers interconnection loss. Digital filtering resources are then allocated to DPD, forming a complementary filtering DPD (CF-DPD) with an asymmetrical filtering function. Since CF-DPD is configured according to the residual distortion spectrum after analog filtering, it avoids unnecessary processing of frequency components that have already been sufficiently suppressed, thereby reducing the required sampling rate and digital processing burden.

2 Proposed linearization architecture with complementary filtering

In this part, we present a detailed explanation of the proposed linearization architecture with a complementary filtering function, focusing on how analog and digital filtering resources are effectively distributed to address nonlinear distortions in PA systems. Fig. 2a illustrates the framework of the traditional linearization architecture. The system consists of multiple discrete RF components, including a PA for signal amplification, a filter to suppress unwanted frequency components, and a coupler to extract feedback signals for the DPD block. Although this structure is straightforward, the interconnections among these components introduce additional insertion loss, degrading system efficiency, and the use of discrete components increases the system's overall circuit size, posing challenges for integration. Besides, the traditional DPD block

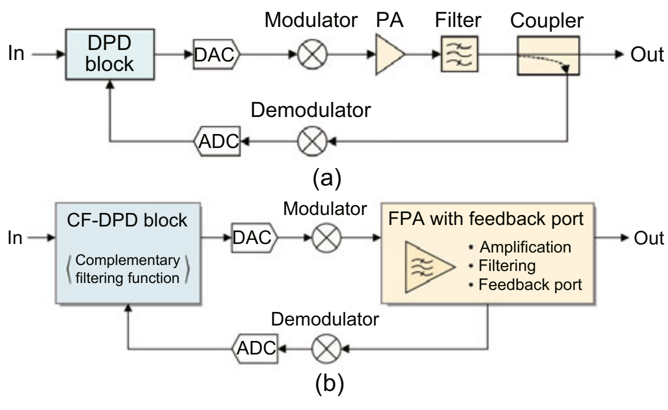

Fig. 2 Linearization architectures for filtering PAs (FPAs): (a) traditional linearization architecture; (b) proposed linearization architecture with complementary filtering. ADC: analog-to-digital converter; DAC: digital-to-analog converter

typically requires a sampling rate five times the signal bandwidth, imposing stringent demands on the analog-to-digital converter (ADC) and digital-to-analog converter (DAC).

To reduce interconnection loss and enhance system integration, our design replaces the traditional PA, filter, and coupler with a filtering power amplifier with integrated feedback port (FPA-FB), as shown in Fig. 2b. From the hardware implementation perspective, by integrating amplification, filtering, and feedback extraction into a single component, the proposed FPA-FB reduces the number of discrete RF components and lowers interconnection loss. More importantly, the integrated filtering response not only suppresses harmonic components but also attenuates part of the IMD before digital correction, thereby providing the hardware basis for the subsequent CF-DPD.

Assuming that FPA-FB suppresses most of the PA distortions, the remaining distortions are confined within the residual bandwidth BW_{res}, as shown in Fig. 3. The proposed DPD block incorporates a complementary filtering function, which is specifically designed to suppress the residual distortion of FPA-FB. From the model perspective, the passband of this complementary filtering function is determined by the residual distortion components after analog filtering, rather than being fixed. By setting the sampling rate to match BW_{res}, the proposed linearization architecture focuses digital correction on the residual distortion requiring further suppression, thereby relaxing the constraints on ADC/DAC sampling rates. This analog–digital coordination allows FPA-FB to define the residual distortion bandwidth through analog filtering, while CF-DPD is configured accordingly for the remaining digital correction.

It is worth noting that the residual bandwidth may not always be perfectly symmetric around the signal center frequency in practical scenarios. Such asymmetry can result from factors like uneven roll-off at the filter edges or frequency shifts introduced during fabrication. Therefore, the complementary filtering function in CF-DPD should be configured according to the spectral allocation of the residual distortion after analog filtering. As illustrated in Fig. 3, the proposed CF-DPD can be regarded as a residual-bandwidth-oriented framework, where the digital correction bandwidth is determined by the residual distortion left after analog filtering rather than being predefined independently in the digital domain. When the residual bandwidth exceeds the bandwidth required by conventional full-band DPD, the proposed CF-DPD degenerates into a conventional DPD solution. Similarly, when the residual distortion bandwidth is symmetrically distributed around the carrier and can be covered by a symmetric band-limited model, the proposed CF-DPD becomes equivalent to traditional BL-DPD.

3 Analog filtering based on FPA-FB

3.1 Structure of the proposed FPA-FB

As previously mentioned, FPA-FB is a multifunctional component that integrates filtering, amplification, and a feedback port. To achieve these functionalities within a minimized footprint, we propose the structure as shown in Fig. 4, which is designed to efficiently combine these functions while maintaining performance. The output circuit of the proposed FPA-FB consists of two components: a multimode BPF and an output matching network (OMN) with an integrated feedback port. Placing the filter before OMN allows it to attenuate most unwanted frequencies in advance, enabling OMN to focus exclusively on the fundamental frequency impedance transformation. This simplification not only reduces the size of OMN but also facilitates the integration of the feedback port, which will be discussed in detail later.

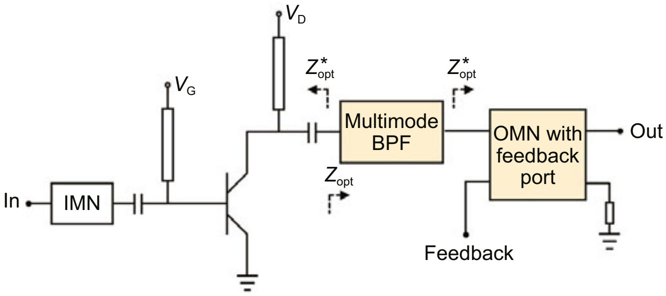

Fig. 4 Overview of the proposed FPA-FB. V_G and V_D denote the gate bias voltage and drain bias voltage, respectively, and Z_{opt} denotes the optimum load impedance of the transistor. IMN: input matching network; BPF: bandpass filter; OMN: output matching network

Herein, analog filtering is realized based on an integrated multimode filter, unlike most filtering PAs (FPAs) in the literature (Joshi et al., 2007; Chen KL et al., 2011, 2013a, 2013b; Li et al., 2013, 2019; Estrada et al., 2021; Gao et al., 2021). Based

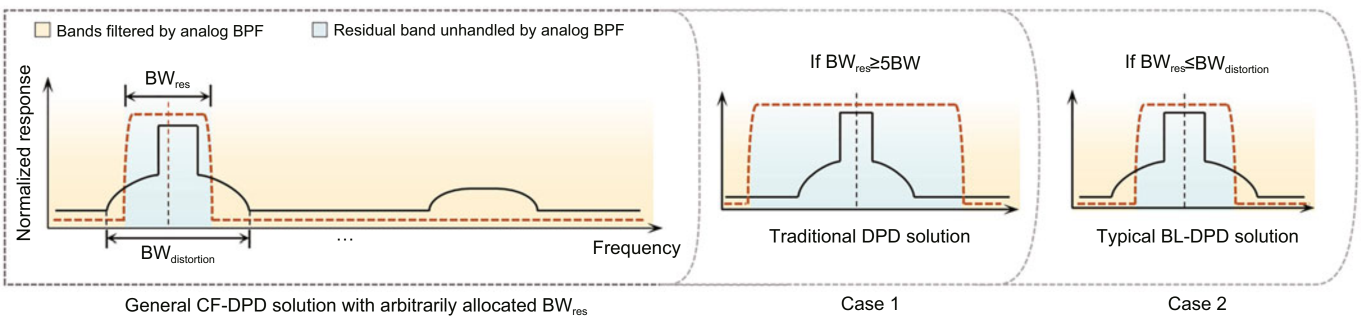

Fig. 3 Proposed CF-DPD solution with arbitrary residual bandwidth and its two special cases. BW is the signal bandwidth, BW_{res} is the residual distortion bandwidth after analog filtering, and $BW_{distortion}$ is the bandwidth of the IMD components generated around the transmission passband

on coupling matrix theory, the output circuits of these FPAs simultaneously achieve impedance transformation and filtering functions. By adjusting two parameters in the coupling matrix, the desired impedance characteristics can be achieved. However, the miniaturization of the overall system using these FPAs may not meet expectations in practice. Two primary factors cause this limitation. First, most FPAs employ cascaded resonators, resulting in a significant increase in circuit size. Second, higher-order modes of these resonators can introduce parasitic passbands and thus lead to inadequate harmonic suppression. Therefore, it may still be necessary to cascade low-pass filters after these FPAs to attenuate harmonics, which contradicts the original intention of reducing size.

Therefore, a multimode BPF with a wide stopband is adopted in this paper. The selection of a multimode filter is driven by its inherent advantage in size reduction over an N-stage cascaded filter, as each multimode resonator effectively functions as multiple individual resonators. Another reason for selecting a multimode BPF is its ability to offer flexible control over resonant frequencies of different modes through various perturbation techniques. With an integrated multimode BPF for suppressing unwanted frequency components and an OMN for impedance transformation and feedback, the proposed FPA-FB achieves a compact size and low insertion loss.

3.2 Filtering realization based on multimode BPF

A semicircular patch resonator is utilized in this paper to design the BPF. Patch resonators offer higher power handling capabilities than microstrip designs and provide easier connectivity than substrate integrated waveguide (SIW) or cavity resonators (Hong and Li, 2004), making them well-suited for this application.

As depicted in Fig. 5, the semicircular patch is grounded by a metallic via, introducing a new resonant mode compared to the conventional patch resonators. The newly introduced mode is referred to as the LC mode; the semicircular patch works as a capacitor, and the metallic via works as an inductor, thus forming an LC resonant unit (Fei et al., 2021). The resonant frequency of the LC mode is lower than that of the fundamental mode in unperturbed patch resonators, resulting in a more compact structure. Modes TM_{100} and TM_{110} are the second and third resonant modes of the grounded semicircular patch, respectively, identical to those in conventional patch resonators. It is worth noting that the introduced metallic via is placed where the electric field distribution of modes 2 and 3 is zero, ensuring that it does not influence the frequencies of these two modes.

In typical filter designs, the impedance at both ends is set to 50 Ω to ensure compatibility with other devices. However, the filter described herein does not perform impedance transformation, so the load impedance at both ends is set to the conjugate of the optimal impedance. Based on the simulated load-pull results, Z_{opt} is selected as (9.8–j·2) Ω taking into account both power-added efficiency (PAE) and output power. Fig. 6 demonstrates the response variations of the patch resonator when the impedance at both ends is set to 50 Ω and Z^*_{opt}. It is evident that the first three resonant modes shift to higher frequencies and exhibit a higher Q-factor. These changes do not introduce new challenges for multimode BPF design. As mentioned earlier, one advantage of a multimode BPF is its ability to flexibly control each resonant frequency through perturbations, making frequency variations less of a concern. For a higher Q-factor, the external Q-value of the resonator can be adjusted by modifying the position and size of the feeder. While a high Q-factor results in increased insertion losses, it also improves the filter's selectivity, making it more effective in suppressing undesired frequencies.

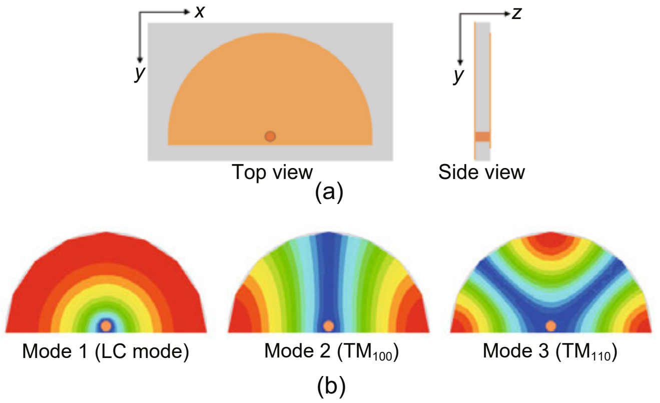

Fig. 5 Grounded patch resonator: (a) structure; (b) electric field distributions of the first three resonant modes

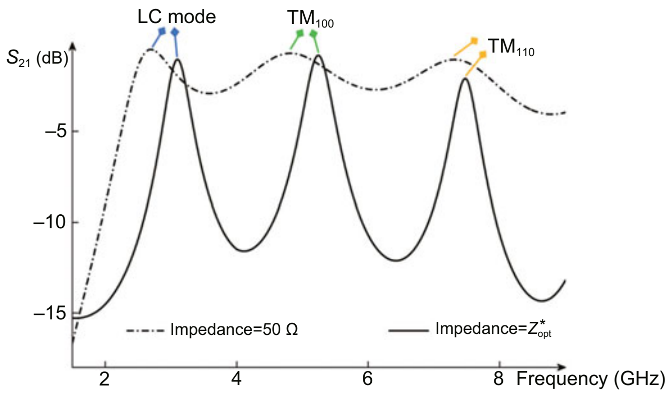

Fig. 6 Response characteristic comparison of a grounded semicircular patch resonator with different impedances

To generate a passband, symmetric slots are introduced to the semicircular patch, as shown in Fig. 7. Based on the current distribution, radially oriented slots have no impact on the current path of mode 1, so the frequency of mode 1 (f_1) remains unchanged. For modes 2 and 3, however, the presence of radial slots extends the current paths, resulting in a decrease in their resonant frequencies. Detailed simulation results under different L_{P} (length of the slot) and θ (angle between the slots) are given in Fig. 8. An increase in L_{P} results in longer current paths for modes 2 and 3, which in turn decreases f_2 and f_3. In addition, when θ is zero, the direction of the slots is perpendicular to the current path of mode 2 and parallel to that of mode 3, so the slots have the maximum influence on the current path of mode 2 and the minimum influence on the current path of mode 3. As θ increases, the effect on the current path of mode 2 decreases, whereas the effect on the current path of mode 3 increases. As a result, f_2 and f_3 exhibit opposite trends as θ changes, allowing for better control of the passband response. Therefore, by carefully adjusting L_P and θ, the bandwidth of BPF can be controlled.

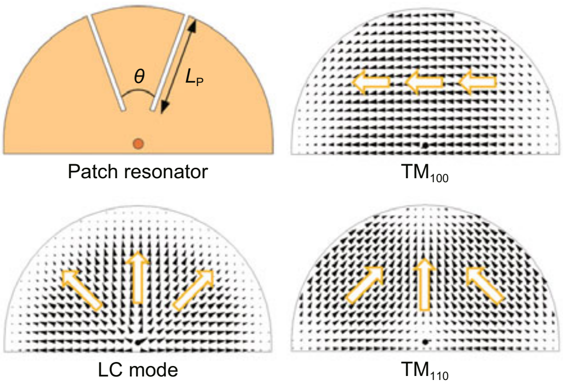

Fig. 7 Etched slots and current distributions of the first three resonant modes

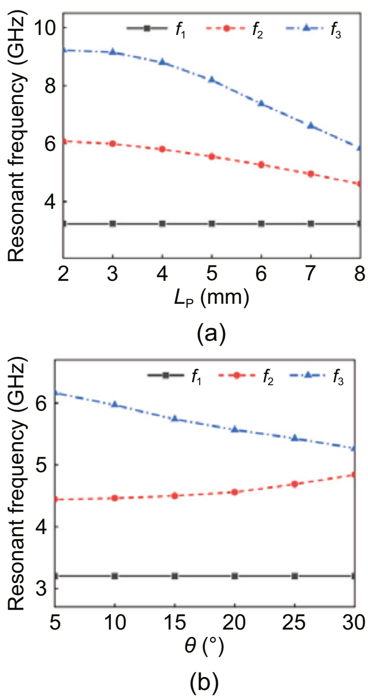

Fig. 8 Simulated frequency variations under changes of L_P (a) and θ (b)

In this paper, the filter bandwidth is designed to slightly exceed 400 MHz, facilitating the transmission of 5G NR broadband signals with bandwidths up to 400 MHz. The simulated response is depicted in Fig. 9, where the filter has a center frequency (f_0) of 3.5 GHz with in-band return losses exceeding 17 dB and insertion losses less than 1.35 dB. Furthermore, the filter exhibits wide stopband suppression, achieving over 15 dBc attenuation from $1.1f_0$ up to $5.7f_0$, thereby effectively suppressing harmonic components of the PA output.

3.3 Feedback realization based on an asymmetrical coupler

With almost all harmonic components blocked from entering OMN, as shown in Fig. 9, the OMN design can focus on transforming impedance at the fundamental frequency, thereby facilitating the simultaneous feedback function.

When the goal is to achieve impedance transformation alongside power coupling, the use of an asymmetric coupler, as shown in Fig. 10, becomes an intuitive option (Tripathi, 1975; Tripathi and Chin, 1982). For DPD, a coupling factor of 30 dB is sufficient in this case, as only minimal power is needed to correct distortion. Since nearly all of the PA output power is delivered to the load through the main line, the effects of the coupled line are negligible. As a result, the characteristic impedance and length of the main line l_1 can be directly determined using Z_{opt} and Z_0 as follows:

$$Z_1 = \sqrt{Z_0 R_{\text{opt}} - \frac{Z_0 X_{\text{opt}}^2}{Z_0 - R_{\text{opt}}}}, \tag{1}$$

$$l_1 = \frac{\lambda}{2\pi} \arctan\left(\frac{Z_0 - R_{\text{opt}}}{Z_0 X_{\text{opt}}} \sqrt{Z_0 R_{\text{opt}} - \frac{Z_0 X_{\text{opt}}^2}{Z_0 - R_{\text{opt}}}} \right), \tag{2}$$

where λ denotes the guided wavelength at the operating frequency, R_{opt} and X_{opt} are the real and imaginary parts of Z_{opt}, respectively, and Z_0 denotes the system reference impedance.

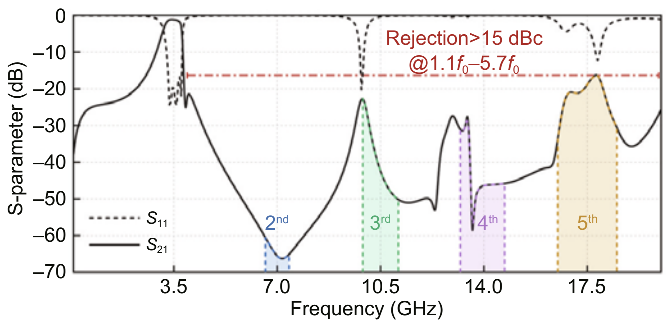

Fig. 9 Simulated filter response with high stopband rejection

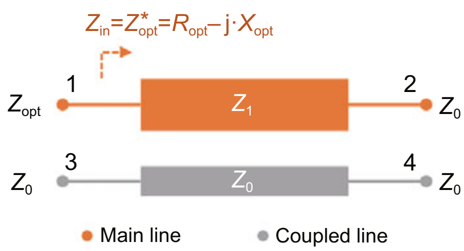

Fig. 10 Output matching circuit with feedback port based on an asymmetrical coupler. Z_{in} denotes the input impedance at port 1

For the coupled microstrip line, port 4 is grounded with a 50 Ω resistor, and port 3 is designated as the feedback port. The coupling factor can be easily determined through electromagnetic simulation by analyzing the distance between the main line and the coupled line. In this paper, the simulated coupling level is approximately 35 dB across 3.3–3.7 GHz, with a variation of less than 0.25 dB. The simulated group delay variation of the feedback path is less than 0.01 ns across the same frequency range. Since only a small fraction of the output power is extracted for feedback observation, the integrated feedback extraction has limited influence on the mainline matching and transmission response.

3.4 Final configuration of the proposed FPA-FB

Fig. 11 presents the final configuration of the proposed FPA-FB. The design employs a TLY-5 substrate with a dielectric constant of 2.2 and a thickness of 0.508 mm. The specified dimensions of the patch filter are θ=7.5°, L_{r}=2.9 mm, L_{s}=2.9 mm, L_x=22 mm, R_{p}=11 mm, W_{r}=0.2 mm, W_{s}=0.2 mm, and W_z=0.64 mm. The bypass capacitors for the source and gate are selected as 10 pF, 39 pF, 100 pF, and 1 μF. Besides, serpentine slots are employed in the multimode filter to further increase the current path. FPA-FB has an overall size of 67 mm×32 mm, equivalent to $1.1\lambda_{\mathrm{g}}\times0.5\lambda_{\mathrm{g}}$. Within such a reduced size, FPA-FB effectively integrates amplification, filtering, and feedback functions, demonstrating its capability for miniaturization.

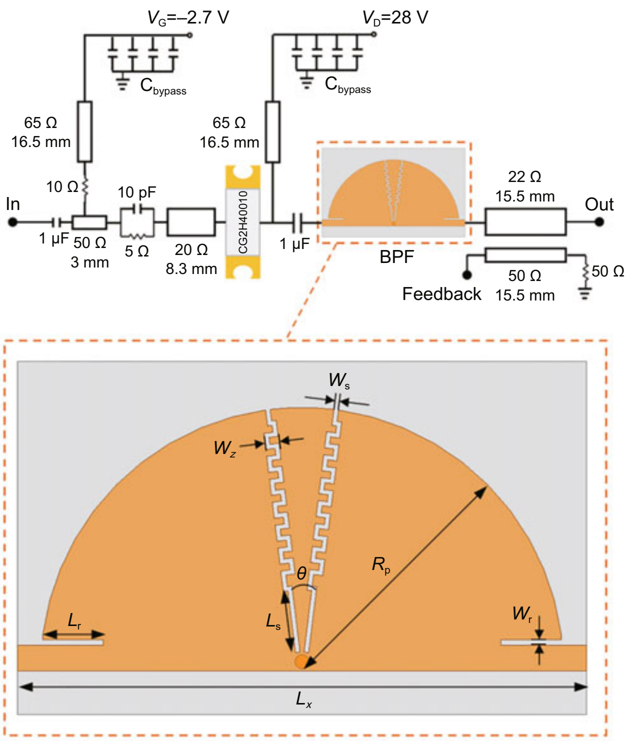

Fig. 11 Final configuration and dimensions of the proposed multifunctional FPA-FB for analog filtering

4 Digital filtering based on CF-DPD

4.1 CF-DPD architecture

To effectively address nonlinearities in PAs, DPD has become a vital digital filtering technique for reducing IMD. Various behavioral models and their corresponding accuracies have been analyzed in Pedro and Maas (2005) and Tehrani et al. (2010), typically requiring data five times the signal bandwidth. Covering a wider band enables the capture of higher-order nonlinear terms, thereby improving modeling accuracy and enhancing overall system performance.

However, for amplifiers combined with BPFs, the accuracy of DPD modeling is notably influenced by the characteristics of the filters. These filters alter the spectral distribution of the output signals, leading to the attenuation of certain IMD components. For example, Volterra series models typically include third-order and fifth-order distortion terms, assuming that these higher-order components are not suppressed. The assumption holds when the filter or system does not attenuate distortion products, enabling an accurate representation of system behavior. However, when a filter attenuates higher-order IMD components, employing a digital filter that matches the actual filter response becomes essential for more realistic compensation of the nonlinearities of the output signal.

In this paper, due to the asymmetric spectrum allocation of our filter, the IMD of FPA-FB will also exhibit an uneven distribution with differing coverage ranges. As shown in Fig. 9, the filter exhibits a transmission zero on the right side of the passband, resulting in steeper roll-off compared to that on the left side. Therefore, in Fig. 12, the residual distortion on the left side of the proposed FPA-FB spans a wider range compared to the right side. This means that the CF-DPD here should employ a filtering function with complementary asymmetrical spectrum allocation. Specifically, the analog filter in FPA-FB and the digital filter in CF-DPD should exhibit the same passband to achieve complementary filtering.

Inspired by the classic band-limited Volterra series model, an asymmetric filtering function with complementary spectrum allocation is introduced to the model. According to previous simulation results, the center frequency of the filter is 3.5 GHz, and the frequencies at which the suppression level reaches 15 dB are 2.70 GHz and 3.85 GHz. In other words, the filter effectively attenuates distortions outside the 2.70–3.85 GHz range, allowing the CF-DPD system to focus solely on distortions within this range. Therefore, employing an asymmetrical baseband filter with a passband from −800 MHz to 350 MHz is sufficient in this paper.

4.2 CF-DPD model

As mentioned earlier, FPA-FB can capture the PA output in real time. Likewise, the DPD algorithm must be capable of swiftly performing nonlinear system modeling and compensation. A widely used model is the generalized memory polynomial (GMP), preferred over the Volterra series for its efficiency in capturing the memory effects of PA systems. With a finite memory depth and polynomial order, the GMP model offers better computational efficiency and is more suitable for real-time applications. The GMP model can be expressed as follows (Morgan et al., 2006):

$$\begin{aligned} y(n) = &\sum_{k=0}^{K_{\mathrm{a}}-1}\sum_{l=0}^{L_{\mathrm{a}}-1} a_{\mathrm{kl}}x(n-l)\left|x(n-l)\right|^{k} \\ &+\sum_{k=1}^{K_{\mathrm{b}}}\sum_{l=0}^{L_{\mathrm{b}}-1}\sum_{m=1}^{M_{\mathrm{b}}} b_{\mathrm{klm}}x(n-l)\left|x(n-l-m)\right|^{k} \\ &+\sum_{k=1}^{K_{\mathrm{c}}}\sum_{l=0}^{L_{\mathrm{c}}-1}\sum_{m=1}^{M_{\mathrm{c}}} c_{\mathrm{klm}}x(n-l)\left|x(n-l+m)\right|^{k}, \end{aligned} \quad (3)$$

where $x(n)$ and $y(n)$ represent the input and output signals, respectively. K_{a}, K_{b}, and K_{c} represent nonlinearity orders,

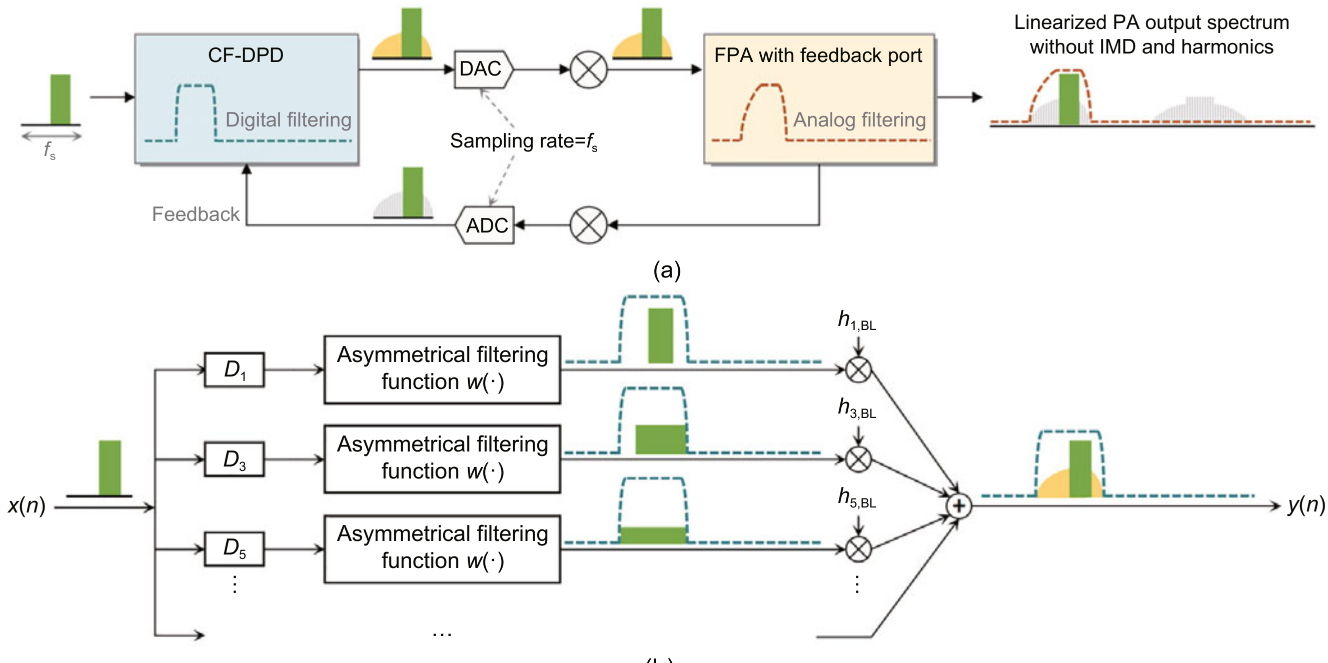

Fig. 12 Architecture and model implementation of the proposed CF-DPD: (a) diagram of the proposed CF-DPD system; (b) asymmetrical filtering function with complementary spectrum allocation in the modified band-limited Volterra series model. D_n denotes the n^{th}-order Volterra operator and $h_{n,\mathrm{BL}}$ denotes the corresponding n^{th}-order band-limited Volterra kernel for odd-order nonlinear terms

L_a, L_b, and L_c represent memory depths, and M_b and M_c are the longest lagging and leading delay tap lengths, respectively. The coefficients a_{kl}, b_{klm}, and c_{klm} correspond to the GMP model applied to the aligned terms, lagging cross-terms, and leading cross-terms, respectively.

Finite impulse response (FIR) filters exhibit symmetry around the zero-frequency point. This is due to the filter's real-valued coefficients. In other words, for a real-valued sequence $h[n]$, the Fourier transform exhibits conjugate symmetry between positive and negative frequencies, i.e., $H(f)=H^*(-f)$. Therefore, introducing complex coefficients can disrupt this symmetry, allowing for the design of a complementary filtering function that effectively suppresses the residual distortion.

Specifically, the inclusion of a complex exponential term $\mathrm{e}^{\mathrm{j}2\pi f_\triangle n/f_\mathrm{s}}$ in the complementary filter design shifts the frequency response of the prototype FIR filter. This operation enables an asymmetric spectral allocation and provides flexibility for matching the residual distortion bandwidth after analog filtering. For clarity, the complementary filtering function is uniformly denoted as $h_{\mathrm{CF}}[n]$. Starting from a prototype FIR low-pass filter $h[n]$, the complementary filtering function can be obtained as

$$h_{\mathrm{CF}}[n]=h[n]\cdot\mathrm{e}^{\mathrm{j}2\pi f_\triangle n/f_\mathrm{s}},\tag{4}$$

where f_s denotes the sampling rate and $f_\triangle$ denotes the frequency shift applied to the prototype FIR filter. In this paper, a 100-tap prototype FIR filter is used. The frequency shift can be selected according to the center of the residual distortion band after FPA-FB.

By introducing the complementary filtering function $h_{\mathrm{CF}}[n]$ to limit the bandwidth of each item of the GMP model, the output of the proposed CF-DPD based on the GMP model, $y_{\mathrm{CF}}(n)$, can be derived as follows:

$$\begin{aligned}y_{\mathrm{CF}}(n)=&\sum_{k=0}^{K_\mathrm{a}-1}\sum_{l=0}^{L_\mathrm{a}-1}a_{\mathrm{kl}}h_{\mathrm{CF}}[n]\left[x(n-l)|x(n-l)|^k\right]\\&+\sum_{k=1}^{K_\mathrm{b}}\sum_{l=0}^{L_\mathrm{b}-1}\sum_{m=1}^{M_\mathrm{b}}b_{\mathrm{klm}}h_{\mathrm{CF}}[n]\left[x(n-l)|x(n-l-m)|^k\right]\\&+\sum_{k=1}^{K_\mathrm{c}}\sum_{l=0}^{L_\mathrm{c}-1}\sum_{m=1}^{M_\mathrm{c}}c_{\mathrm{klm}}h_{\mathrm{CF}}[n]\left[x(n-l)|x(n-l+m)|^k\right].\end{aligned}\tag{5}$$

Based on the analysis above, employing an asymmetrical baseband filter with a passband from −800 MHz to 350 MHz is sufficient in this case, resulting in a system sampling rate of 1.15 giga samples per second (GSPS). In contrast, if a traditional FIR filter with symmetric frequency allocation is utilized, the frequency range will be extended to −800 MHz to 800 MHz, thereby increasing the system sampling rate to 1.6 GSPS. As a result, the complementary filtering function should be designed based on the frequency distribution of the residual bandwidth after the integrated analog filter. This ensures modeling accuracy and linearization performance while keeping the sampling rate at a minimum. It should be noted that the 1.15-GSPS value derived above represents a conservative design estimate based on the simulated 15-dBc suppression boundary of FPA-FB. This value illustrates the sampling rate reduction enabled by the asymmetric complementary filtering function compared with BL-DPD. In a practical implementation, the final sampling rate is determined according to the measured residual distortion bandwidth that remains after analog filtering.

5 Experimental results

5.1 Continuous wave measurement results of the FPA-FB

The proposed FPA-FB is fabricated and measured to verify the design concept. Fig. 13a shows a photograph of the fabricated FPA-FB along with its frequency response under 28 V drain voltage and −2.7 V gate voltage. The results indicate good agreement between simulation and measurement. FPA-FB delivers a small-signal gain of approximately 14.5 dB in the passband, which is commendable considering that our design integrates amplification, filtering, and feedback functionalities. This further demonstrates its effectiveness in reducing interconnect losses. The transmission coefficient across the entire frequency band is further presented in Fig. 13b. The measured transmission coefficient S_{21} achieves suppression levels exceeding 43 dBc for the 2^{nd} to 5^{th} harmonic components. These results demonstrate that the proposed FPA-FB not only performs well within the target bandwidth but also effectively mitigates higher-order harmonic interference, thereby enhancing the overall linearity of the system.

The frequency characteristics of FPA-FB under large signal excitation are given in Fig. 14a, where the input signal is 28.5 dBm. The measured output power ranges from 38.7 dBm to 40.5 dBm, the gain is between 8.4 dB and 11.9 dB, and the saturated PAE is in the range of 42.6%–52.1% across the frequency range of 3.3–3.7 GHz. The responses of FPA-FB under different output power levels are shown in Fig. 14b, which further supports PA's ability to achieve good performance at both the center and edges of the passband.

Table 1 provides a comparison with other reported FPAs. The proposed design offers balanced performance in terms of efficiency, harmonic suppression, and size reduction while uniquely incorporating a feedback port, which has seldom been realized together in earlier reports. Such an integration not only benefits compact hardware and enhanced linearization capability but also provides direct support for DPD implementation.

5.2 DPD test of 400-MHz wideband modulated signal

The above test results are based on continuous wave measurements, demonstrating that the proposed FPA-FB achieves high efficiency and multi-functionality with a miniaturized circuit size. To further validate the effectiveness of CF-DPD with a complementary filtering function for enhanced broadband linearity, a DPD test platform is established, as illustrated in Fig. 15. The test platform employs an SMW200A vector signal generator, which is synchronized with the signal analyzer using a shared reference clock during the measurement. A 5G

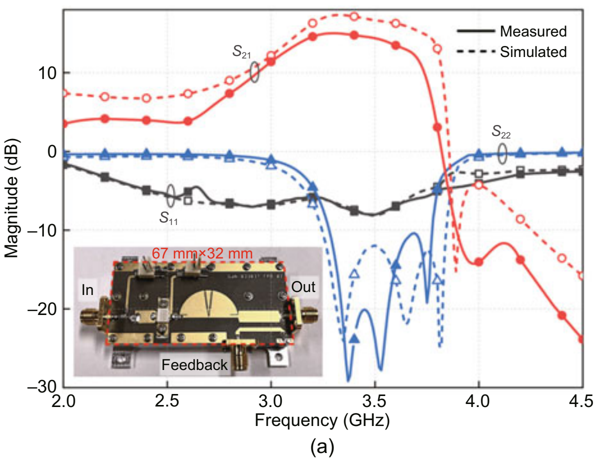

N^{th}-order harmonic	2^{nd}	3^{rd}	4^{th}	5^{th}
Suppression level (dBc)	53	48	43	44

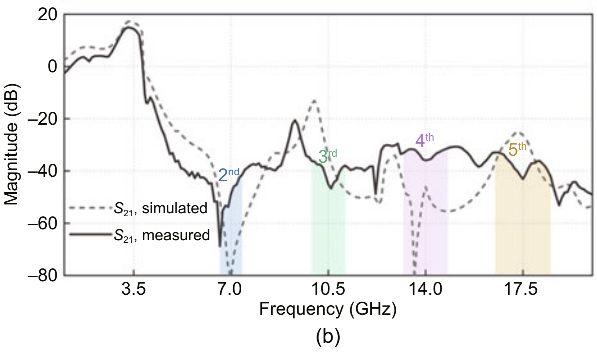

Fig. 13 Frequency-response characterization of the fabricated FPA-FB: (a) simulated and measured S-parameters; (b) broadband transmission characteristics and harmonic suppression

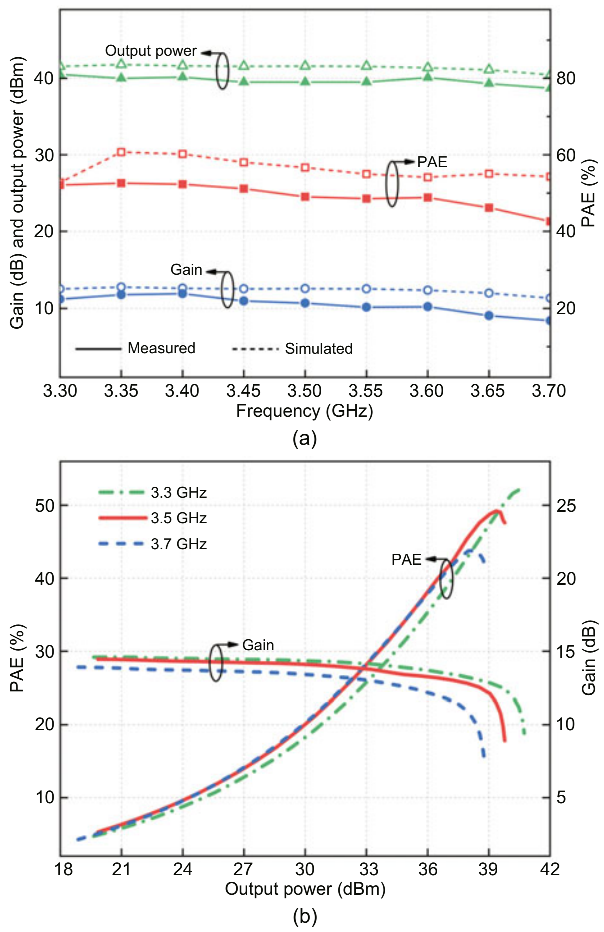

Fig. 14 Large-signal performance of the fabricated FPA-FB: (a) simulated and measured PAE, gain, and output power at saturation; (b) PA performance versus output power at the center and edges of the passband

Table 1 Comparison with other FPAs in the literature

Work	Technology	BW (GHz)	PAE (%)	Harmonic rejection	Size ($\lambda_g \times \lambda_g$)	Feedback port
Chen KL et al. (2013a)	GaN	2.98–3.07	50–71	NM	0.9×0.5	No
Chen KL et al. (2011)	GaN	1.24–1.28	63–76	60 dBc up to 3rd	0.35×0.16	No
Estrada et al. (2021)	GaN	4.5–4.9	38–55	NM	2.3×1.7	No
Li et al. (2019)	GaN	1.6–2.1	63–73	51 dBc up to 4th	0.5×0.4	No
Li et al. (2013)	LDMOS	2.57–2.67	41–46	20 dBc up to 2nd	1.5×1.1	No
This work	GaN	3.3–3.7	43–52	43 dBc up to 5th	1.1×0.5	Yes

NM: not mentioned

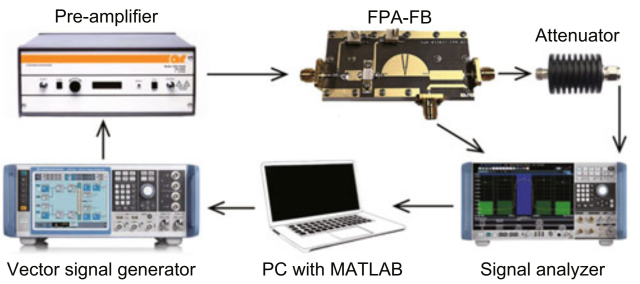

Fig. 15 Overview of the experimental DPD test bench setup

NR signal with a 400-MHz bandwidth and a peak to average power ratio (PAPR) of 8 dB is used in this test. The average power delivered to the PA is 22 dBm, and the corresponding average output power is 34.2 dBm. In this setup, the feedback signal for DPD is directly extracted from the integrated feedback port of FPA-FB and sent to the signal analyzer.

As discussed in Section 4, the implementation of complementary filtering helps reduce the system's sampling rate. Therefore, the PA is linearized using three approaches for comparison: traditional DPD, BL-DPD, and the proposed CF-DPD with an asymmetric filtering function. For all three DPD tests, the signal analyzer is configured with sufficient acquisition bandwidth to ensure consistent waveform acquisition. The DPD coefficients are extracted offline using an iterative indirect learning architecture with seven adaptation iterations. For each DPD case, 40 000 samples are used for coefficient extraction, and approximately 10 000 additional samples are used for validation. All the three tests are based on the GMP model, with the same model parameters for each. The nonlinearity order and memory depth for the aligned signal are K_a=6 and L_a=10. For the lagging and leading signal terms, the nonlinearity orders are K_b=K_c=5, memory depths are L_b=L_c=4, and the longest lagging and leading delay tap lengths are M_b=M_c=4.

The performance comparison of the three DPD models is presented in Table 2. It can be observed that the ACLR reaches −34.7/−39.0 dBc even without applying DPD, highlighting the contribution of the integrated analog filter in enhancing linearity. The proposed CF-DPD achieves optimal normalized mean square error (NMSE) and ACLR while maintaining the minimal oversampling ratio (OSR). Since the same GMP model parameters are used for all three DPD methods, the computational cost per sample is kept comparable for a fair comparison. Therefore, the reduction in OSR corresponds to a reduction in the sampling-rate-related digital processing burden. For the 400-MHz signal, the proposed CF-DPD reduces the equivalent sampling rate from 2.0 GSPS for traditional DPD and 1.0 GSPS for BL-DPD to 850 mega samples per second (MSPS), corresponding to a 57.5% reduction in the processing rate compared with traditional DPD and a 15% reduction compared with BL-DPD.

Table 2 Performance and complexity for the 400-MHz 5G NR signal

Method	Coefficient	NMSE (dB)	ACLR (dBc)	OSR
Without DPD	NA	−15.2	−34.7/−39.0	NA
Traditional DPD	220	−30.5	−40.6/−45.0	5
BL-DPD	220	−32.1	−44.9/−46.7	2.5
Proposed CF-DPD	220	−32.2	−45.1/−47.2	2.125

NA: not available

Fig. 16 presents the output power spectrum for different DPD methods. The black curve represents the measured residual distortion spectrum after the analog filtering response of FPA-FB and before digital correction. Owing to the asymmetric roll-off of the integrated filter, the residual distortion is not symmetrically distributed around the carrier. The red curve further indicates that using the traditional DPD to model the PA with filtering characteristics leads to inaccuracies. As mentioned before, this is due to the fact that the filter integrated within the amplifier modifies the spectral distribution of the output signal, resulting in truncation of the IMD components. Thus, the traditional DPD model fails to properly capture this incomplete IMD effect, leading to an inaccurate representation of the system. BL-DPD exhibits enhanced performance compared to traditional DPD, accompanied by a reduction in sampling rate requirements. This improvement arises from the better alignment of the models with FPA-FB's response characteristics, enabling more precise correction of nonlinear distortions. The proposed CF-DPD with a complementary filtering function delivers the best performance because it achieves the

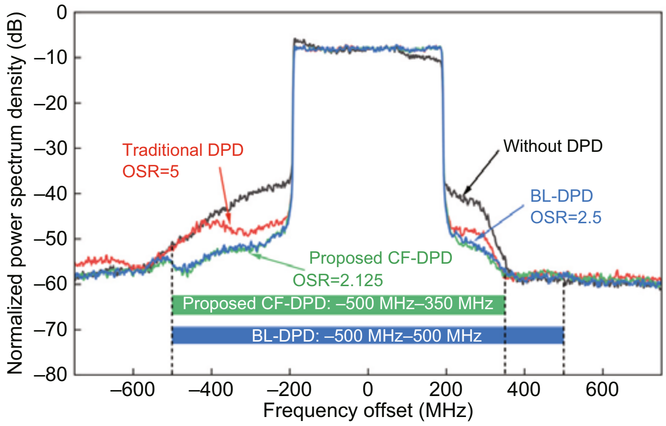

Fig. 16 Output power spectrum for different DPD models

highest alignment with the spectrum allocation of FPA-FB. The passband of the complementary filtering function is set from −500 MHz to 350 MHz according to the measured residual distortion spectrum after analog filtering. Therefore, the proposed CF-DPD operates at the lowest implemented equivalent complex-baseband sampling rate of 850 MSPS, corresponding to an OSR of 2.125 with respect to the 400-MHz signal bandwidth. The amplitude-to-amplitude (AM/AM) and amplitude-to-phase (AM/PM) characteristics before and after the proposed CF-DPD are shown in Fig. 17. These measurement results highlight the potential of co-designed CF-DPD and FPA-FB for broadband linearization.

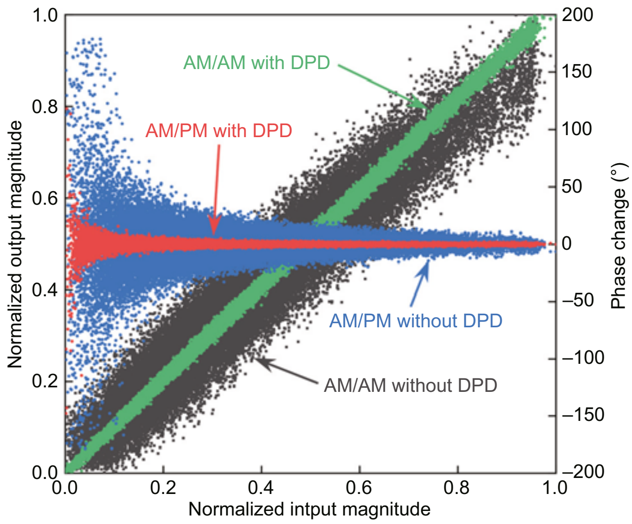

Fig. 17 AM/AM and AM/PM characteristics for the 400-MHz 5G NR signal before and after the proposed CF-DPD

6 Conclusions

This paper proposes a linearization architecture aimed at enhancing broadband linearity based on the complementary filtering concept. A FPA-FB is co-designed with a CF-DPD to realize the architecture. The integration of a multimode BPF and a feedback-enabled output matching network facilitates efficient harmonic suppression, size reduction, and multifunctionality, providing a compact and versatile solution. Experimental results validate that FPA-FB effectively suppresses harmonic distortion, and that the proposed CF-DPD model not only reduces IMD but also minimizes the sampling rate requirements of the DPD system, making the proposed architecture efficient for high-linearity broadband signal processing.

Acknowledgments

This work was supported by the Scientific Research Innovation Capability Support Project for Young Faculty (No. SRICSPYF-ZY2025020).

Author contributions

Huihui FEI designed the research and drafted the paper. Yucheng YU assisted with the experimental validation and measurements. Peng CHEN and Chao YU revised and finalized the paper.

Conflict of interest

All the authors declare that they have no conflict of interest.

Data availability

The data that support the findings of this study are available from the corresponding author upon reasonable request.

Declaration on the use of generative AI tools

During the preparation of this work, the authors used DeepSeek to improve language. After using this tool, the authors reviewed and edited the content as needed and take full responsibility for the content of the published article.

References

3GPP, 2024a. NR; NR and NG-RAN Overall Description; Stage 2. 3GPP TS 38.300 Version 16.17.0.

3GPP, 2024b. NR; User Equipment (UE) Radio Transmission and Reception; Part 1: Range 1 Standalone. 3GPP TS 38.101-1 Version 17.12.0.

Chen KL, Liu XG, Chappell WJ, et al., 2011. Co-design of power amplifier and narrowband filter using high-Q evanescent-mode cavity resonator as the output matching network. IEEE MTT-S Int Microwave Symp, p.1-4. https://doi.org/10.1109/MWSYM.2011.5972854

Chen KL, Lee J, Chappell WJ, et al., 2013a. Co-design of highly efficient power amplifier and high-Q output bandpass filter. *IEEE Trans Microw Theory Techn*, 61(11):3940-3950. https://doi.org/10.1109/TMTT.2013.2284485

Chen KL, Lee TC, Peroulis D, 2013b. Co-design of multi-band high-efficiency power amplifier and three-pole high-Q tunable filter. *IEEE Microw Wirel Compon Lett*, 23(12):647-649. https://doi.org/10.1109/LMWC.2013.2283876

Chen SZ, Kang SL, 2018. A tutorial on 5G and the progress in China. *Front Inform Technol Electron Eng*, 19(3):309-321. https://doi.org/10.1631/FITEE.1800070

Estrada JA, Montejo-Garai JR, de Paco P, et al., 2021. Power amplifiers with frequency-selective matching networks. *IEEE Trans Microw Theory Techn*, 69(1):697-708. https://doi.org/10.1109/TMTT.2020.3020097

Fei HH, Wang YY, Zhang Q, et al., 2021. Miniaturized single-/dual-band bandpass filters based on grounded square patch resonator with controllable passbands. *Microw Opt Technol Lett*, 63(6):1688-1692. https://doi.org/10.1002/mop.32793

Gao Y, Zhang F, Qiao YY, et al., 2021. A microstrip filter direct-coupled amplifier based on active coupling matrix synthesis. *Front Inform Technol Electron Eng*, 22(9):1260-1269. https://doi.org/10.1631/FITEE.2000292

Hong JS, Li S, 2004. Theory and experiment of dual-mode microstrip triangular patch resonators and filters. *IEEE Trans Microw Theory Techn*, 52(4):1237-1243. https://doi.org/10.1109/TMTT.2004.825653

Joshi H, Sigmarsson HH, Peroulis D, et al., 2007. Highly loaded evanescent cavities for widely tunable high-Q filters. IEEE/MTT-S Int Microwave Symp, p.2133-2136. https://doi.org/10.1109/MWSYM.2007.380346

Katz A, Wood J, Chokola D, 2016. The evolution of PA linearization: from classic feedforward and feedback through analog and digital predistortion. *IEEE Microw Mag*, 17(2):32-40. https://doi.org/10.1109/MMM.2015.2498079

Li YC, Wu KC, Xue Q, 2013. Power amplifier integrated with bandpass filter for long term evolution application. *IEEE Microw Wirel Compon Lett*, 23(8):424-426. https://doi.org/10.1109/LMWC.2013.2268457

Li YC, Chen QC, Xue Q, et al., 2019. Filtering power amplifier with wide bandwidth using discriminating coupling. *IEEE Trans Circ Syst I Regul Pap*, 66(10):3822-3830. https://doi.org/10.1109/TCSI.2019.2913025

Liang D, Zhang H, Wang YT, et al., 2025. Design of oscillator-based reconfigurable modulator with high-Q FBAR resonators supporting fast OOK/BFSK/BPSK modulation. *IEEE Trans Circ Syst I Regul Pap*, 72(6):2543-2555. https://doi.org/10.1109/TCSI.2025.3559727

Liu X, Lv GS, Wang DH, et al., 2020. Energy-efficient power amplifiers and linearization techniques for massive MIMO transmitters: a review. *Front Inform Technol Electron Eng*, 21(1):72-96. https://doi.org/10.1631/FITEE.1900467

Menendez S, de Paco P, Villarino R, et al., 2006. Closed-form expressions for the design of ladder-type FBAR filters. *IEEE Microw Wirel Compon Lett*, 16(12):657-659. https://doi.org/10.1109/LMWC.2006.885610

Morgan DR, Ma Z, Kim J, et al., 2006. A generalized memory polynomial model for digital predistortion of RF power amplifiers. *IEEE Trans Signal Process*, 54(10):3852-3860. https://doi.org/10.1109/TSP.2006.879264

Nam S, Koohi MZ, Peng WH, et al., 2021. A switchless quad band filter bank based on ferroelectric BST FBARs. *IEEE Microw Wirel Compon Lett*, 31(6):662-665. https://doi.org/10.1109/LMWC.2021.3069880

Othmani M, Boulejfen N, Turunen M, et al., 2023. Parallel delta-sigma modulator-based digital predistortion of wideband RF power amplifiers. *IEEE Trans Circ Syst I Regul Pap*, 70(2):705-718. https://doi.org/10.1109/TCSI.2022.3218295

Park SJ, Reines I, Rebeiz G, 2009. High-Q RF-MEMS tunable evanescent-mode cavity filter. IEEE MTT-S Int Microwave Symp Digest, p.1145-1148. https://doi.org/10.1109/MWSYM.2009.5165904

Pedro JC, Maas SA, 2005. A comparative overview of microwave and wireless power-amplifier behavioral modeling approaches. *IEEE Trans Microw Theory Techn*, 53(4):1150-1163. https://doi.org/10.1109/TMTT.2005.845723

Ruppel CCW, 2017. Acoustic wave filter technology—a review. *IEEE Trans Ultrason Ferroelectr Freq Contr*, 64(9):1390-1400. https://doi.org/10.1109/TUFFC.2017.2690905

Ruppel CCW, Reindl L, Weigel R, 2002. SAW devices and their wireless communications applications. *IEEE Microw Mag*, 3(2):65-71. https://doi.org/10.1109/MMW.2002.1004053

Tehrani AS, Cao HY, Afsardoost S, et al., 2010. A comparative analysis of the complexity/accuracy tradeoff in power amplifier behavioral models. *IEEE Trans Microw Theory Techn*, 58(6):1510-1520. https://doi.org/10.1109/TMTT.2010.2047920

Tripathi VK, 1975. Asymmetric coupled transmission lines in an inhomogeneous medium. *IEEE Trans Microw Theory Techn*, 23(9):734-739. https://doi.org/10.1109/TMTT.1975.1128665

Tripathi VK, Chin YK, 1982. Analysis of the general nonsymmetrical directional coupler with arbitrary terminations. *IEE Proc H (Microw Opt Antenn)*, 129(6):360-362. https://doi.org/10.1049/ip-h-1.1982.0072

Wood J, 2017. System-level design considerations for digital predistortion of wireless base station transmitters. *IEEE Trans Microw Theory Techn*, 65(5):1880-1890. https://doi.org/10.1109/TMTT.2017.2659738

Yu C, Guan L, Zhu EN, et al., 2012. Band-limited Volterra series-based digital predistortion for wideband RF power amplifiers. *IEEE Trans Microw Theory Techn*, 60(12):4198-4208. https://doi.org/10.1109/TMTT.2012.2222658

Zhu AD, 2015. Decomposed vector rotation-based behavioral modeling for digital predistortion of RF power amplifiers. *IEEE Trans Microw Theory Techn*, 63(2):737-744. https://doi.org/10.1109/TMTT.2014.2387853

Zhu XE, Lee V, Phillips J, et al., 2009. An intrinsically switchable FBAR filter based on barium titanate thin films. *IEEE Microw Wirel Compon Lett*, 19(6):359-361. https://doi.org/10.1109/LMWC.2009.2020013